Exceptional gettering response of epitaxially grown kerfless silicon

Citation: Powell, D. M. et al. "Exceptional Gettering Response of Epitaxially Grown Kerfless Silicon." Journal of Applied Physics 119, 6 (February 2016): 065101 © 2016 AIP Publishing LLC

As Published: http://dx.doi.org/10.1063/1.4940947

Publisher: American Institute of Physics (AIP)

Persistent URL: http://hdl.handle.net/1721.1/118899

Version: Final published version: final published article, as it appeared in a journal, conference proceedings, or other formally published context

Exceptional gettering response of epitaxially grown kerfless silicon

D. M. Powell,[1,a)] V. P. Markevich,[2] J. Hofstetter,[1] M. A. Jensen,[1] A. E. Morishige,[1] S. Castellanos,[1] B. Lai,[3] A. R. Peaker,[2] and T. Buonassisi[1,b)]
[1]*Massachusetts Institute of Technology, Cambridge, Massachusetts 02139, USA*
[2]*Photon Science Institute, The University of Manchester, Manchester M13 9PL, United Kingdom*
[3]*Advanced Photon Source, Argonne National Laboratory, Argonne, Illinois 60439, USA*

(Received 25 November 2015; accepted 6 January 2016; published online 8 February 2016)

The bulk minority-carrier lifetime in *p*- and *n*-type kerfless epitaxial (epi) crystalline silicon wafers is shown to increase >500× during phosphorus gettering. We employ kinetic defect simulations and microstructural characterization techniques to elucidate the root cause of this exceptional gettering response. Simulations and deep-level transient spectroscopy (DLTS) indicate that a high concentration of point defects (likely Pt) is "locked in" during fast (60 °C/min) cooling during epi wafer growth. The fine dispersion of moderately fast-diffusing recombination-active point defects limits as-grown lifetime but can also be removed during gettering, confirmed by DLTS measurements. Synchrotron-based X-ray fluorescence microscopy indicates metal agglomerates at structural defects, yet the structural defect density is sufficiently low to enable high lifetimes. Consequently, after phosphorus diffusion gettering, epi silicon exhibits a higher lifetime than materials with similar bulk impurity contents but higher densities of structural defects, including multicrystalline ingot and ribbon silicon materials. Device simulations suggest a solar-cell efficiency potential of this material >23%. © *2016 AIP Publishing LLC*. [http://dx.doi.org/10.1063/1.4940947]

I. INTRODUCTION

Approximately 90% of solar cells manufactured today are wire-sawn from crystalline silicon (c-Si) ingots.[1] During the squaring and wire-sawing and wafer-preparation processes, approximately 50% of the starting silicon is removed.[2,3] A variety of "kerfless" wafering approaches have been proposed to eliminate cutting loss, mostly relying on additive manufacturing approaches to grow wafers from gaseous or molten silicon.[4] These technologies aspire to lower costs by reducing silicon usage (grams of silicon per watt) and increase scalability by reducing process complexity and factory footprint. In principle, kerfless silicon approaches may also enable substrates of arbitrary thickness and lateral dimensions, *in-situ* depth-dependent doping, and in-line substrate manufacturing for silicon.[5]

To be competitive in the photovoltaic industry, kerfless wafering approaches must also enable high solar-cell conversion efficiencies.[3,6] To support high efficiencies, high post-gettering bulk minority-carrier lifetimes are required.[7] Recently, excellent estimated bulk lifetimes >1 ms have been reported for gettered *p*- and *n*-type epitaxially grown kerfless silicon (epi).[8,9] This high lifetime is surprising, given that other kerfless technologies historically exhibited lower cell efficiencies than multicrystalline silicon (mc-Si) and Czochralski (CZ) benchmarks.[10] Fundamental studies are needed to explain why this material behaves differently from other kerfless wafers.

Herein, we examine the root cause(s) of exceptional gettering response of kerfless epi wafers. We find that in the specific material studied herein, as-grown lifetime is suppressed by the presence of a metallic point defect; however, lifetime improves dramatically with gettering. We attribute this behavior in part to the rapid cooling rate during growth, which "locks in" a high density of extrinsic point defects. While this effect can suppress as-grown lifetimes, fast-diffusing point defects are readily removed during gettering, resulting in highly improved gettered lifetimes. The low density of competitive internal gettering sites (i.e., structural defects) is believed to be a pre-requisite to the exceptional gettering response.

II. MATERIALS AND METHODS

Epitaxial wafers are grown to a thickness of approximately 100 μm on recrystallized porous silicon substrates at 1100 °C (growth rate >4 μm/min). Both *p*-type (boron-doped 1.8 Ω cm) and *n*-type (phosphorous-doped 0.4 Ω cm) wafers are studied. After growth, wafers are exfoliated and cleaned with a CP4 etch (quenched with HF, 30% KOH 1 min, and HF). As-grown lifetime is measured with a Sinton WCT-120 tester in quasi-steady-state photoconductance (QSSPC) mode. Nine data points, instead of the default five, are employed in the QSSPC calculation of the time derivative of injection level to reduce noise. A 20 nm Al_2O_3 film passivates the surfaces and is deposited with thermal atomic layer deposition (ALD), as detailed in Ref. 9. The interstitial iron concentration ($[Fe_i]$) in *p*-type epi wafers is determined with the technique of Fe_i-B_s pair dissociation and lifetime measurements.[9,11] As-grown material is set aside for deep level transient spectroscopy (DLTS) and synchrotron micro-X-ray fluorescence (μ-XRF) microscopy.

Both *p*-type and *n*-type samples are gettered in a phosphorous ($POCl_3$) tube diffusion furnace (Tystar Titan 3800), as detailed in Ref. 9. Two recipes are applied with a plateau

a)dmpowell@alum.mit.edu
b)buonassisi@mit.edu

temperature of 845 °C. The first consists of a standard (STD) high-throughput process with furnace unloading directly at the plateau temperature. The second process includes an extended cooling process and low temperature anneal (EXT) for enhanced point-defect reduction in the wafer bulk.[12] Lifetime (and [Fe_i] for *p*-type) is again measured on gettered material after Al_2O_3 passivation. Gettered material was also set aside for DLTS and etch-pit density (EPD) measurements.

For DLTS, 1 mm diameter Schottky diodes are formed on the *n*-type samples by thermal evaporation of Au and on *p*-type samples by plasma sputtering of Ti through a shadow mask. A layer of Al(Au) is evaporated onto the back side of the samples to form an ohmic contact. Approximately 4–5 diodes are analyzed on each sample. Current-voltage and capacitance-voltage (*C-V*) measurements at different temperatures are carried out to evaluate the quality of the diodes, to determine the concentration of uncompensated shallow acceptors/donors, and to determine the electric field distribution in the depletion region. Deep electronic levels are characterized with conventional DLTS and Laplace DLTS (L-DLTS) techniques.[13]

Samples are analyzed with synchrotron-based μ-XRF microscopy at Beamline 2-ID-D of the Advanced Photon Source (APS) at Argonne National Laboratory. Conditions included a 10 keV beam with a spot size of approximately 200 nm at full width half maximum at a step size of 220 nm with a dwell time of 1 s. For the configuration used in our measurements, μ-XRF is capable of detecting particles with $K\alpha$ absorption edge energies <10 keV, in both *p*- and *n*-type mc-Si, down to approximately 8 nm in radius for Fe.[14,15,54,55] μ-XRF samples are defect-etched[16] to generate etch-pits that are used for location during the measurement.

To reveal structural defects in the material as etch-pits, samples are etched using a procedure proposed by Sopori.[16] Samples are scanned with an optical microscope and high-resolution flatbed scanner. Defect densities are assessed with an image processing algorithm discussed in Ref. 17. For a qualitative comparison of structural defect populations, *p*-type wafers of a "standard" (i.e., not "high-performance")[18] mc-Si ingot from a commercial vendor are extracted from a center brick, at approximately 90% ingot height. The mc-Si material was subjected to phosphorus diffusion gettering and was passivated with an Al_2O_3/SiN_x stack before lifetime analysis.

III. RESULTS

A. Effective passivated lifetimes

Effective, as-grown, lifetimes of the kerfless epi samples in this study are measured to be <1 μs after surface passivation, in contrast to lifetime values for mc-Si ingots typically measured to be ~2–100 μs for *p*-type, and up to 300 μs for *n*-type. Passivated effective lifetimes after EXT gettering increase to >300 μs with *p*-type and >800 μs with *n*-type epi material at 10^{15} cm^{-3} injection level.[9] Figure 1 shows a notable lifetime improvement after EXT gettering in both *n*- and *p*-type epi materials. Note that for advanced heterojunction devices, the relevant injection level at maximum power point

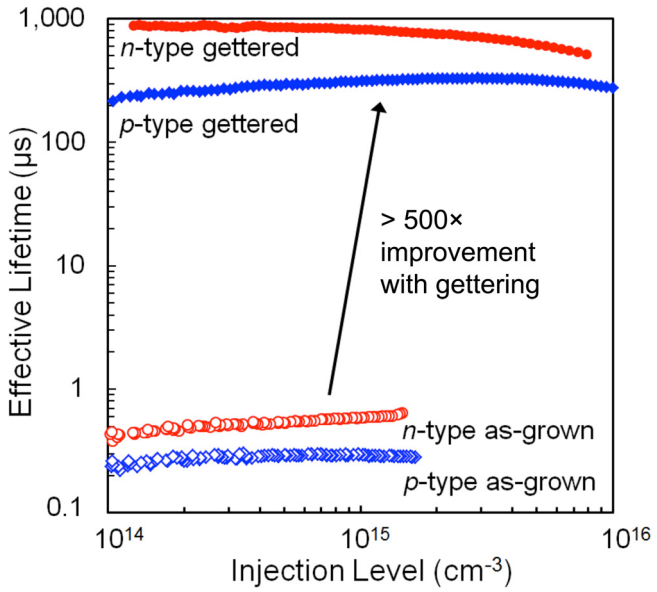

FIG. 1. Injection-dependent effective lifetimes for *n*- and *p*-type epi c-Si, before and after EXT gettering. A notable lifetime improvement is observed in both materials, suggesting that the primary as-grown performance-limiting defects are getterable.

is approximately 10^{14} cm^{-3}, where a bulk lifetime of ~150 μs in *p*-type silicon is predicted to enable device efficiencies of ~23%.[53] Sections III B–III D assess the root cause(s) of this lifetime improvement.

Injection-dependent lifetime measurements are conducted on *p*-type epi to determine interstitial iron ([Fe_i]) concentrations.[21] Lifetime above the carrier lifetime cross-over point[22] is measured with Fe_i-B_s pairs broken by illumination, and then subsequently after re-association as described in Ref. 9. The concentration of iron is then calculated with the model of Macdonald[23] with $\sigma_n = 5.0 \times 10^{-15}$ cm^2 and $\sigma_p = 3.0 \times 10^{-15}$ cm^2 for Fe_i–B_s pairs and $\sigma_n = 1.3 \times 10^{-14}$ cm^2 and $\sigma_p = 7.0 \times 10^{-17}$ cm^2 for Fe_i.[21,22] The estimated bulk lifetime, and measured Fe_i concentrations, of *p*-type samples with Fe_i-B_s pairs broken before and after gettering is compared with the theoretical lifetime entitlement due to intrinsic limits[24] and Fe_i.[25] The results do not differ significantly from those presented in Ref. 9: [Fe_i] in as-grown material is estimated to be $\sim(4.5 \pm 75) \times 10^{11}$ cm^{-3} (large uncertainty due to low signal); $(2.5 \pm 1) \times 10^{10}$ cm^{-3} for standard gettering; and $(3 \pm 7) \times 10^{9}$ cm^{-3} for extended gettering (large uncertainty due to low change in lifetime).

Sentaurus device simulations indicate that this material is capable of high cell efficiencies of >23%.[53] This estimate aligns with experience, as cell efficiencies have reached 22.5% with *n*-type epi material using a heterojunction with intrinsic thin-layer (HIT) architecture.[26]

B. Defect etching

A low bulk structural defect density is known to improve the gettering response in silicon materials for photovoltaics.[44,52] After defect etching, samples of (a) *p*-type mc-Si and (b) *n*-type epi are compared in Figure 2 using a high-resolution flatbed scanner. The *n*-type epi material is

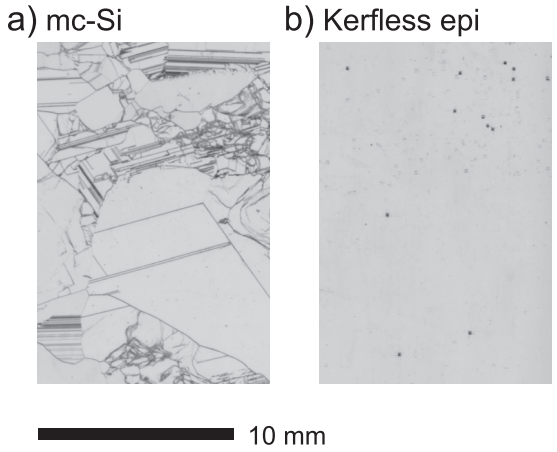

FIG. 2. High-resolution flatbed scanner images comparing representative regions of (a) a mc-Si ingot and (b) single-crystalline kerfless epi silicon. Defect etching reveals an average dislocation density of $\leq 10^4\,cm^{-2}$ for the epi, and $10^5\,cm^{-2}$ for mc-Si.

revealed to be single crystalline with EPD of $\leq 10^4\,cm^{-2}$, and approximately comparable etch-pit density is observed in *p*-type epi material. We note that $10^4\,cm^{-2}$ is generally considered benign with respect to solar-cell performance.[19] In contrast, standard mc-Si exhibits EPD of $10^5\,cm^{-2}$ or higher. At these densities, solar-cell performance is generally reduced,[19] although electrical impact can vary with dislocation character and impurity decoration.[20]

C. Deep level transient spectroscopy

1. p-type epitaxial silicon

C-V analysis on Schottky diodes with as-grown *p*-type material shows that the uncompensated acceptor concentration is in the range of $(8–10) \times 10^{15}\,cm^{-3}$. Using four-point probe, the measured average doping concentration is $8.5 \times 10^{15}\,cm^{-3}$ for the analyzed wafer.[9] Figure 3 shows a typical DLTS spectrum for a *p*-type sample from this material. Two peaks with their maxima at about 53 K and 168 K and similar magnitudes dominate the spectrum of as-grown material (spectrum 1, black). In the following, we will refer to the traps responsible for the above peaks as H(0.09) and H(0.32), where H indicates a hole trap, and the numbers are the values of activation energy for hole emission in eV. Our analysis shows that the concentrations of the H(0.09) and H(0.32) traps are nearly equal in the samples studied and are in the range from 3×10^{13} to about $1.2 \times 10^{14}\,cm^{-3}$ with some variations along the epi slice. The equality of the concentrations of the H(0.09) and H(0.32) traps indicates that these could be two energy levels of the same defect. L-DLTS measurements in the temperature ranges of 50–60 K and 160–190 K are completed for a detailed analysis of hole emission processes from the dominant traps. Figure 4 shows examples of the L-DLTS spectra recorded. It is found that in both temperature ranges, the L-DLTS spectra consist of a single sharp emission line. Such a line shape indicates that (i) hole emission is from point-like defects, and (ii) the level of strain in the material is either low or uniform throughout the material.[13]

A strong electric-field-induced enhancement of hole emission rate for the H(0.09) trap occurs as can be seen in

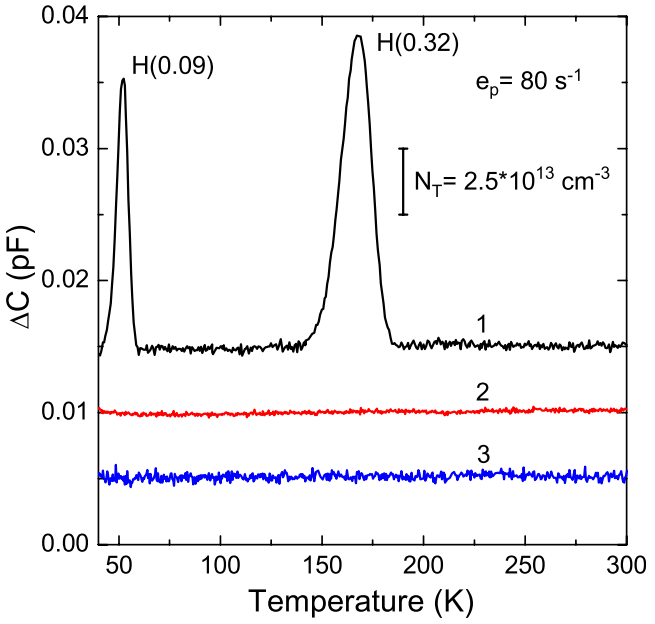

FIG. 3. DLTS spectra for as-grown *p*-type epi material show the presence of two peaks corresponding to Pt_s (1, black). After standard (2, red) and extended (3, blue) gettering, the peaks are no longer above detection limits. Measurement settings were: bias $-9.0 \rightarrow -7.0$ V for spectrum 1, bias $-9.0 \rightarrow -4.0$ V for spectra 2 and 3, emission rate $e_p = 80\,s^{-1}$, and pulse duration 1 ms for all the spectra. The spectra are shifted on the vertical axis for clarity.

Figure 5. Therefore, the electronic signatures (activation energy for hole emission [E_h] and pre-exponential factor (α)) for the H(0.09) trap has been determined at the lowest possible value of electric field ($E \approx 1 \times 10^4$ V/cm) and L-DLTS signal magnitude has been used when determining the trap concentration in the samples studied.[13,27] Figure 6 shows Arrhenius plots of T^2-corrected hole emission rates for the

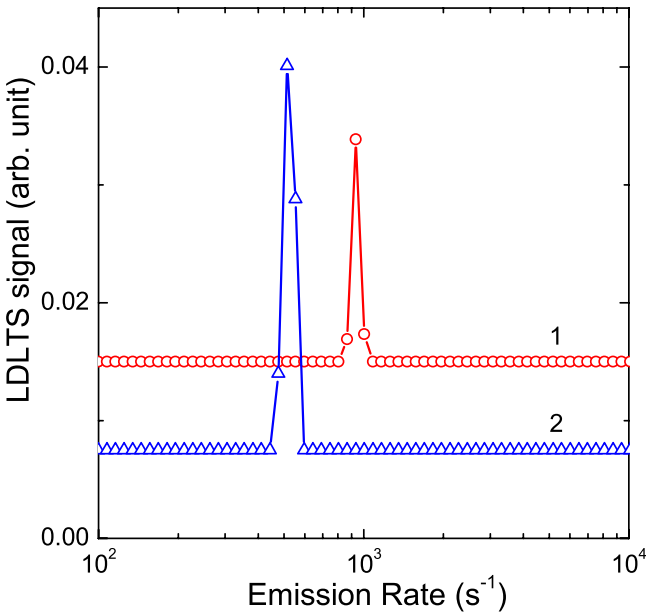

FIG. 4. Laplace DLTS spectra for *p*-type epi material, measured at (1) 53 K and (2) 180 K on an as-grown sample. Measurement settings were: bias -1.0 to -0.2 V for spectrum 1, bias -9.0 to -4.0 V for spectrum 2, and pulse duration 1 ms for both spectra. Spectra are shifted on the vertical axis for clarity.

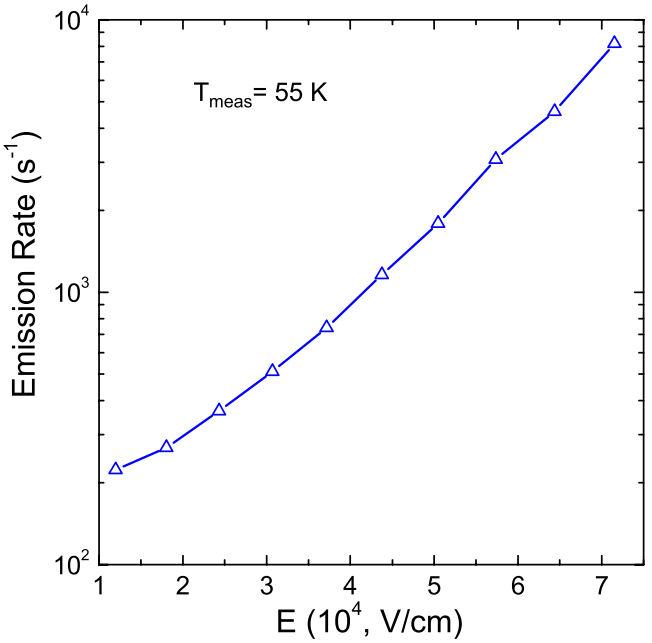

FIG. 5. Dependence of the hole emission rate from the H(0.09) trap versus electric field strength in the depletion region of a reverse-biased ($V_b = -9.5$ V) Schottky diode on *p*-type epi. Values of the electron emission rate have been determined from the LDLTS spectra, which were recorded with the application of the double L-DLTS technique.[13]

H(0.09) and H(0.32) traps measured with the use of the L-DLTS technique. The Arrhenius plot and electronic signatures for the H(0.32) trap ($E_h = 0.322 \pm 0.001$ eV, $\alpha = 1.7 \times 10^7\ s^{-1}\ K^{-2}$) are very close to those for the first donor level of platinum in silicon.[27–29] It is thought that platinum has two donor levels in the lower part of the Si band gap.[28,31,32] Thus, in Figure 6, we have compared the Arrhenius plot for the H(0.09) trap ($E_h = 0.089 \pm 0.001$ eV, $\alpha = 8.8 \times 10^6\ s^{-1}\ K^{-2}$) with that plotted for the second donor level of platinum according to the most reliable data from literature ($E_h = 0.08$ eV, $\alpha = 8 \times 10^5\ s^{-1}\ K^{-2}$).[28,31] The plots differ slightly. The difference between the Arrhenius plots is thought to be caused by the electric-field-induced enhancement of hole emission rate for the H(0.09) trap. In summary, the data obtained on electronic signatures and concentrations of the H(0.09) and H(0.32) indicate that these traps are consistent with the two donor levels of platinum.

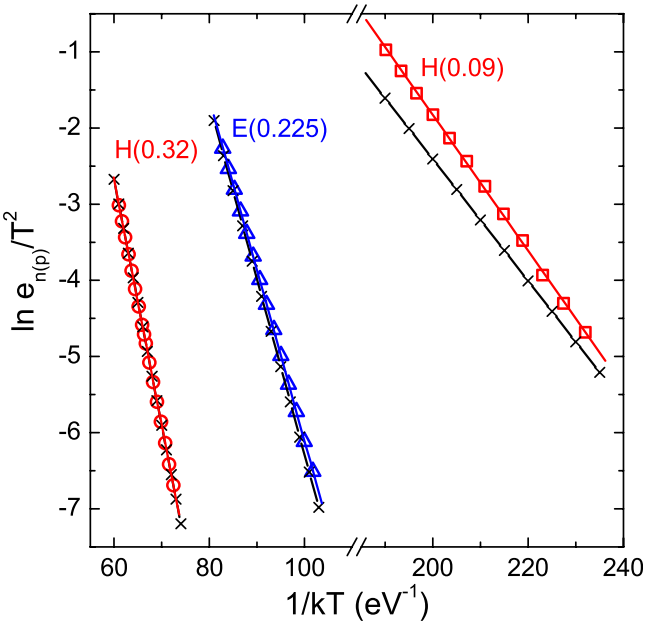

FIG. 6. DLTS Arrhenius plots of *p*-type epi material, indicating the presence of substitutional platinum defects. Arrhenius plots of T^2-corrected hole and electron emission rates for the dominant traps observed in the DLTS spectra of as-grown *p*-type (red) and *n*-type (blue) kerfless epi-Si shown. Arrhenius plots for hole and electron emission rates for energy levels of Pt impurity atoms in Si according to the data from Refs. 28–31 are shown by black crosses.

Further evidence for Pt being the dominant defect is found from an analysis of the DLTS spectra recorded with bias/pulse settings for studying the regions close to the surface of the samples. Such regions of Schottky diodes on *p*-type Si samples usually contain some hydrogen atoms introduced during diode processing. In the DLTS spectra for subsurface regions of the samples, an additional trap H(0.39) ($E_h = 0.389 \pm 0.002$ eV, $\alpha = 2.1 \times 10^6\ s^{-1}\ K^{-2}$) has been observed. This trap can be associated with an energy level of Pt-H_2 complex.[32]

The DLTS spectra 2 and 3 in Figure 3 are recorded on two slices from the kerfless epi *p*-type wafer used in this study, which are subjected to the standard (spectrum 2, red) and extended (spectrum 3, blue) gettering procedures, respectively. There are no detectable signals in the DLTS spectra of the gettered samples. Both the standard and extended gettering procedures resulted in removal (within the DLTS detection limit of about $5 \times 10^{11}\ cm^{-3}$ in this case) of the electrically active defects from the slices.

2. n-type epitaxial silicon

An analysis of the *C-V* dependences recorded on Schottky diodes on as-grown *n*-type kerfless epi slices shows an uncompensated donor concentration in the range of $(5–6) \times 10^{15}\ cm^{-3}$. Using four-point probe, the measured doping concentration is higher at $9.8 \times 10^{15}\ cm^{-3}$ for the analyzed wafer. Figure 7 shows a conventional DLTS spectrum for a sample from this material. A peak with its maxima at about 121 K {E(0.225) trap} dominates the as-grown spectrum (1, black), and two minor peaks with their maxima at about 152 K and 255 K {E(0.487) trap} can be seen. The concentration of the E(0.225) trap is in the range of $(2-4) \times 10^{13}\ cm^{-3}$ with some variations along the epi slice. Depth concentration profiles for the E(0.225) and E(0.487) traps can be seen in Figure 8. It is seen from the depth profiles that the E(0.487) traps are located in narrow subsurface ($\leq 1.2\ \mu m$) regions of the samples. The L-DLTS spectra recorded in the temperature range 110–140 K have shown just one sharp electron emission line related to the E(0.225) trap as in the case of the dominant traps in *p*-type epi-Si samples. It can be stated from the analysis of the L-DLTS line shape that the E (0.225) trap is related to an energy level of a point defect, and the material is not strained. An Arrhenius plot of the T^2-corrected electron emission rates for the E(0.225) trap measured with the use of L-DLTS technique is shown in Figure 6 and the derived electronic signatures for the trap are $E_e = 0.225 \pm 0.001$ eV and

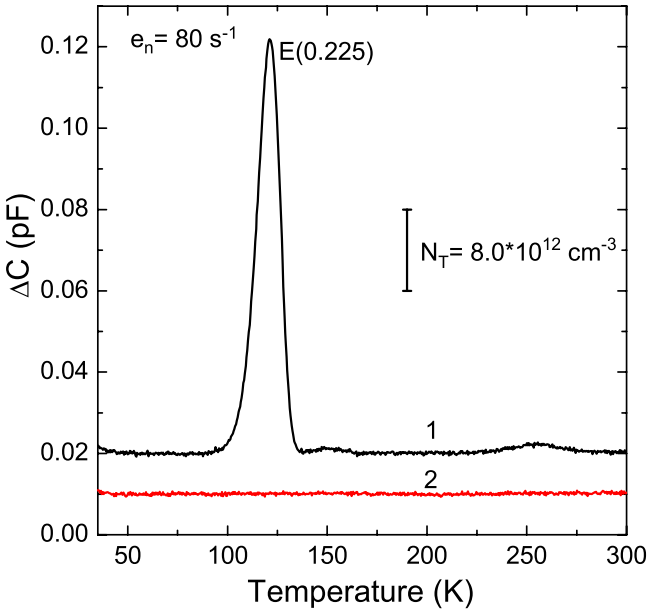

FIG. 7. DLTS spectra for Schottky diodes on *n*-type epi samples: Results on as-grown (1, black), and standard gettered (2, red) material are shown. Gettering removes detectable peaks from the *n*-type material. Measurement settings were: $e_n = 80\,s^{-1}$, bias −9.0 to −4.0 V, and pulse duration 1 ms. The spectra are shifted on the vertical axis for clarity.

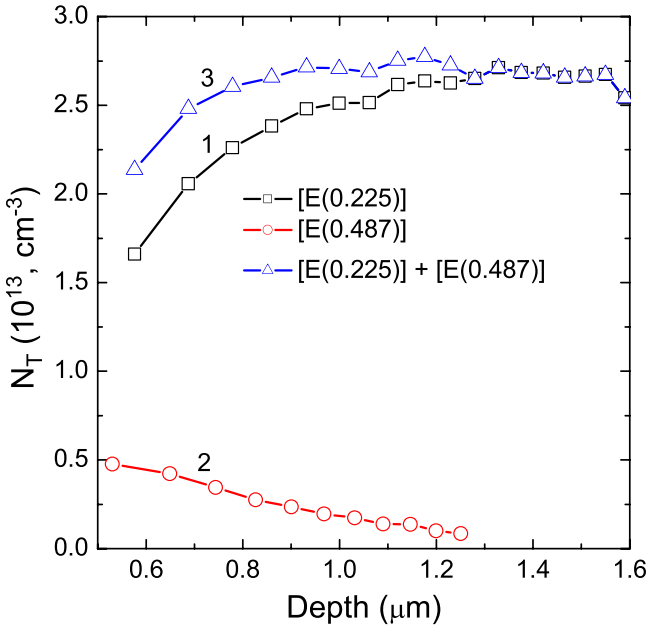

FIG. 8. Concentration depth profiles of the E(0.225) and E(0.487) traps in as-grown kerfless epi-Si:P samples: (1, black) E(0.225) trap, (2, red) E(0.487) trap, and (3, blue) the sum of the concentrations of the E(0.225) and E(0.487) traps. Profiles were taken at 130 K for the E(0.225) trap and at 260 K for the E(0.487) trap with reverse bias varied from −10 V to −1 V and filling pulse voltage varied from −9 V to 0 V with 1 V difference between the bias and pulse voltages.

$\alpha = 1.3 \times 10^7\,s^{-1}\,K^{-2}$. The Arrhenius plot and electronic signatures for the E(0.225) trap are very close to those for the first acceptor level of platinum in silicon.[28,30] Electronic signatures of the E(0.487) trap ($E_h = 0.487 \pm 0.001$ eV, $\alpha = 6.75 \times 10^6\,s^{-1}\,K^{-2}$) are close to those for an energy level of the Pt-H center.[32] The depth profile of the concentration of the E(0.487) trap (Fig. 8) is consistent with its assignment to the Pt-H center.

The DLTS spectrum 2 (red) in Figure 7 is recorded on a sample from the kerfless epi *n*-type slice that is subjected to the standard gettering procedure. As in the case in *p*-type material, there are no visible signals in the DLTS spectrum of the gettered sample. The standard gettering process results in removal (within the DLTS detection limit of about $5 \times 10^{11}\,cm^{-3}$ in this case) of the electrically active defects from both the epi *n*-type and *p*-type slices.

D. Synchrotron micro X-ray florescence

Figure 9 shows a $20 \times 20\,\mu m^2$ synchrotron-based μ-XRF map taken near a stacking fault in the as-grown *p*-type wafer studied herein. Particles containing Ti, Fe, Cr, Cu, and Zn are observed. The presence of these elements is also observed with inductively coupled plasma mass spectrometry.[9] We note that Pt is unobservable with the 10 keV beam, as it has *K* and *L* X-ray absorption edges >10 keV.[15] Similarly, μ-XRF maps of an as-grown *n*-type epi wafer (not shown) have revealed the presence of Ni-rich particles (presumably precipitates) at stacking faults. Compared to the elements such as Ti and Zn, Ni is a fast diffuser in silicon at high temperatures and is therefore easily gettered.[33]

The size of the largest iron particle observed in the map is assessed with the assumption of spherical particles[34,35] and a density of iron in precipitated form of $C_{Fe,p} = 2.63 \times 10^{22}$ atom/cm^3.[36] The resulting estimated maximum particle radius for Fe is 16 nm. The largest titanium particle in the map was calculated with the same method as iron, but with $C_{Ti,p} = 3.23 \times 10^{22}$ atom/cm^3.[36] The resulting radius is 49 nm. While larger than the observed iron precipitate, the size of the titanium precipitate is smaller than inclusions observed in mc-Si.[35]

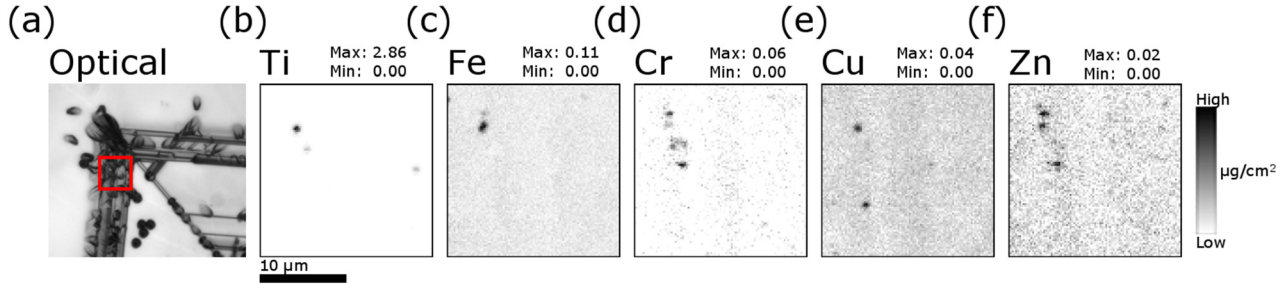

FIG. 9. Synchrotron-based μ-XRF analysis of as-grown *p*-type material. (a) At a stacking fault, particles of (b) Ti, (c) Fe, (d) Cr, (e) Cu, and (f) Zn are observed. The approximate scanned area is indicated in red in the optical image (a). The maximum radius of Fe particles observed in the sampled area is 16 nm.

IV. DISCUSSION

The as-grown lifetime in the epitaxial material is low (Figure 1), despite the single-crystal structure and low structural defect density of the material (Figure 2). Lifetime spectroscopy and modeling indicate that Fe_i does not limit as-grown lifetime in *p*-type material, as the estimated bulk lifetimes fall significantly below the calculated expectation due to the measured Fe_i concentration, consistent with the previous reports.[9] Synchrotron-based μ-XRF (Figure 9) suggests the presence of metal-rich particles (Ti, Fe, Cr, Cu, Ni, Zn) at structural defects in this epi material. Because of the low structural-defect density in this epi sample, it is unlikely that these defects regulate as-grown lifetime (in this sample). However, DLTS (Figures 3–7) indicates the presence of $>10^{13}\,cm^{-3}$ Pt point defects in the as-grown material, sufficient to limit the as-grown lifetime to $<1\,\mu s$, per Shockley-Read-Hall (SRH) kinetics modeling.[25,28] Pt is used as an electrode material during porous silicon etching because of its good stability in hydrofluoric acid,[37] and Pt has previously been observed to contaminate epitaxial wafers for solar cells.[37] Thus, it is likely that while metal-rich particles may locally lower the minority-carrier lifetime, the homogeneously distributed regions of low lifetime are likely caused by a high density of Pt point defects.

High as-grown point-defect concentrations may be facilitated in epitaxially grown material because of two effects. First, the lack of solid-liquid segregation during growth, and fast cooling to room temperature. In silicon crystals grown from melt, a strong solid-liquid segregation purifies the growing crystal. The segregation coefficient for many 3*d* transition metals ranges from $k_{eff} = 10^{-8}$ to 10^{-5}, meaning that only a fraction of 10^{-8} to 10^{-5} of the contaminants present in the melt are incorporated into the ingot.[39] This phenomenon allows the feedstock materials for traditional ingot silicon to be far more contaminated than acceptable levels in wafers.[40] In principle, because epitaxial materials benefit from avoiding contact between both molten and solidified silicon (in the case of mc-Si) with crucible walls (a source for contamination[41]), as-grown contamination levels should be reduced by implementing more stringent impurity controls throughout the process.

Second, the fast cooling to room temperature "locks in" extrinsic contaminants in point-defect form, resulting in lower as-grown lifetimes. An epitaxial wafer is cooled from growth temperatures at approximately 60 °C/min.[45,46] This is far faster than the approximately 2 °C/min cooling rate employed by ingot mc-Si.[46,47] Simulations of iron precipitation during crystal cooling applying Ham's law[48] as modified by Hieslmair *et al.*[49] at these two cooling rates indicate that 77% of the original total concentration of iron is in interstitial form in epi, while only 0.2% of iron is found in interstitial form in mc-Si.[45] These results are consistent with the as-grown mc-Si materials where 0.1% to 10% of total iron is found in interstitial form.[50] Simulation parameters included an initial total iron concentration of $3.5 \times 10^{13}\,cm^{-3}$, $C_{Fep} = 2.63 \times 10^{22}\,cm^{-3}$,[36] the initial precipitate radius $r_0 = 1.5 \times 10^{-6}\,cm$, and the density of precipitate sites $N = 10^8\,cm^{-3}$.[51] μ-XRF analysis, however, indicates that the observed maximum precipitate radius of Fe in the epi sample is 16 nm (Figure 9). This is consistent with the observed as-grown Fe precipitate radii in mc-Si and is above the measurement detection limits of approximately 8 nm.[14] Because of the detection limits, however, precipitates of $r_{Fep} < 8$ nm could be present in the sample.[56–58]

After gettering, the lifetime improves notably in both *n*- and *p*-type epi materials (Figure 2). The large lifetime increase and the low structural defect density indicate that the defect responsible for limiting as-grown lifetimes have been removed during gettering.[9] Our DLTS analysis indicates that gettering reduces the peaks we associate with Pt contamination to below our detection limit ($\sim 5 \times 10^{11}\,cm^{-3}$) in both *p*- and *n*-type materials (Figures 3 and 7). This observation is substantiated by literature data suggesting that Pt is getterable in c-Si; the $\sqrt{4Dt}$ diffusion distance of Pt at 845 °C for 25 min is $\sim 68\,\mu m$.[38] SRH modeling indicates that the low point-defect concentrations are consistent with the high observed gettered lifetimes.[46] Furthermore, the lack of large precipitates (because of fast cooling during growth) implies that gettering proceeds swiftly, without the kinetic limitation of dissolving precipitates.[43]

Finally, as with as-grown material, lifetime spectroscopy and SRH recombination modeling indicate that Fe_i is not the primary performance-limiting defect in gettered *p*-type material. Further confirmation is provided by the extended gettering process where Fe_i concentrations were effectively reduced in the material, but lifetime did not improve.[9]

V. CONCLUSIONS

Both *p*- and *n*-type kerfless epitaxial silicon exhibit unusually strong responses to phosphorus diffusion gettering. The gettered estimated bulk lifetimes are >1 ms in both *p*- and *n*-type epi,[8,9] a $>500\times$ lifetime improvement with gettering. This lifetime improvement is an order of magnitude larger than that of standard mc-Si, which is typically $\leq 100\times$.

A combination of DLTS, synchrotron-based μ-XRF, and lifetime spectroscopy is used to determine the root cause for this effect. The exceptional gettering response in epi silicon can be attributed to these three factors: First, the defect that limits as-grown lifetime, likely Pt point defects as found from our DLTS measurements, is a fast diffuser and can be easily removed during gettering. (Conversely, there is a low concentration of slowly diffusing point defects.) Second, rapid cooling intrinsic to epi growth increases the proportion of the total contamination present in point-defect form.[42] While this suppresses as-grown lifetimes, the fine dispersion of impurities results in faster and more effective gettering, as opposed to kinetically limited precipitate dissolution prevalent in ingot materials.[43] Third, the low density of extended defects in the epi material facilitates gettering, as there are fewer competitive internal gettering sites.[44] Note that previous ribbon Si materials also had fast cooling rates, but did not benefit from low dislocation density, thus gettered lifetimes were limited to values far below a millisecond.[10]

With the millisecond minority-carrier lifetimes resulting from the exceptional gettering response, device simulations

indicate that epi silicon could support cell efficiencies in excess of 23%, consistent with the recent achievement of a 22.5% epi device.[26]

ACKNOWLEDGMENTS

We thank J. Z. Lee (MIT) for assistance in sample preparation, and D. P. Fenning and A. J. Akey (MIT) for helpful discussions. This work was supported primarily by the U.S. Department of Energy (DOE) under Contract No. DE-EE0005314, and additionally by the National Science Foundation (NSF) and the DOE under NSF CA No. EEC-1041895. D.M.P. and A.E.M. acknowledge the support of the Department of Defense through the National Defense Science and Engineering Graduate Fellowship Program; J.H. acknowledges the support of the Alexander von Humboldt foundation through a Feodor Lynen postdoctoral fellowship; and M. A. Jensen acknowledges support by the National Science Foundation Graduate Research Fellowship Program under Grant No. 1122374. Use of the Advanced Photon Source at Argonne National Laboratory was supported by the U.S. Department of Energy, Office of Science, Office of Basic Energy Sciences, under Contract No. DE-AC02-06CH11357. This work was performed in part at the Center for Nanoscale Systems, a member of the National Nanotechnology Infrastructure Network, which was supported by the NSF under No. ECS-0335765. We also thank the UK Science and Engineering Research Council for support of the DLTS work.

[1]H. Forstner, S. Bandil, M. Zwegers, R. Bollen, G. Coletti, W. Sinke, J. Bultman, P. Wyers, R. Wertz, S. Wu, K. Lin, A. Metz, M. Meixner, M. Fischer, T. Spiess, M. Mette, A. Mette, K. Petter, A. Gerlach, P. Engelhart, G. Xing, A. Demenik, D. McMullen, C. Mohr, A. Stassen, J. Slufcik, L. Yong, S. Kaufmann, Y. Wan, W. Wang, S. Liu, A. Richter, R. Pai, K. Wang, B. Chen, A. Luan, I. Buchovskaja, B. Spill, R. Pingel, A. Ramakrishnan, S. Julsrud, W. Osborne, A. Flores, P. Fath, H. Nussbaumer, S. Raithel, S. Pingel, O. Frank, J. Zhu, A. Ristow, L. Oberbeck, and G. Demenik, *International Technology Roadmap for Photovoltaic (ITRPV) 2013 Results - Revision 1* (Semiconductor Equipment and Materials International, 2014).
[2]A. C. Goodrich, P. Hacke, Q. Wang, B. Sopori, R. Margolis, T. L. James, and M. Woodhouse, Sol. Energy Mater. Sol. Cells **114**, 110 (2013).
[3]D. M. Powell, M. T. Winkler, A. C. Goodrich, and T. Buonassisi, IEEE J. Photovoltaics **3**, 662 (2013).
[4]T. F. Ciszek, J. Cryst. Growth **66**, 655 (1984); G. Hahn and A. Schönecker, J. Phys.: Condens. Matter **16**, R1615 (2004).
[5]K. Van Nieuwenhuysen, I. Gordon, T. Bearda, C. Boulord, M. Debucquoy, V. Depauw, F. Dross, J. Govaerts, S. Granata, R. Labie, X. Loozen, R. Martini, B. O'Sullivan, H. S. Radhakrishnan, K. Baert, and J. Poortmans, in *Proceedings of the 38th IEEE Photovoltaic Specialists Conference*, Austin, TX (2012), p. 001833.
[6]D. M. Powell, M. T. Winkler, H. J. Choi, C. B. Simmons, D. Berney Needleman, and T. Buonassisi, Energy Environ. Sci. **5**, 5874 (2012).
[7]G. Coletti, Prog. Photovoltaics **21**, 1163 (2013).
[8]H. Ruiying, T. S. Ravi, V. Siva, J. Vatus, D. Miller, J. Custodio, K. Moyers, C. Chia-Wei, A. Upadhyaya, and A. Rohatgi, in *Proceedings of the 40th IEEE Photovoltaic Specialist Conference*, Denver, Colorado (2014), p. 2978.
[9]D. M. Powell, J. Hofstetter, D. P. Fenning, R. Hao, T. S. Ravi, and T. Buonassisi, Appl. Phys. Lett. **103**, 263902 (2013).
[10]A. Augusto, D. Pera, H. J. Choi, P. Bellanger, M. C. Brito, J. Maia Alves, A. M. Vallêra, T. Buonassisi, and J. M. Serra, J. Appl. Phys. **113**, 083510 (2013); K. Nakayashiki, V. Meemongkolkiat, and A. Rohatgi, IEEE Trans. Electron Devices **52**, 2243 (2005).
[11]D. H. Macdonald, L. J. Geerligs, and A. Azzizi, J. Appl. Phys. **95**, 1021 (2004).
[12]M. D. Pickett and T. Buonassisi, Appl. Phys. Lett. **92**, 122103 (2008); M. Rinio, A. Yodyunyong, S. Keipert-Colberg, Y. P. B. Mouafi, D. Borchert, and A. Montesdeoca-Santana, Prog. Photovoltaics **19**, 165 (2011).
[13]L. Dobaczewski, A. R. Peaker, and K. Bonde Nielsen, J. Appl. Phys. **96**, 4689 (2004).
[14]D. P. Fenning, J. Hofstetter, M. I. Bertoni, G. Coletti, B. Lai, C. del Canizo, and T. Buonassisi, J. Appl. Phys. **113**, 044521 (2013).
[15]See http://www.ruppweb.org/Xray/elements.html for X-ray Absorption Edge Energies (last accessed December 16, 2014).
[16]B. L. Sopori, J. Electrochem. Soc. **131**, 667 (1984).
[17]D. B. Needleman, H. Choi, D. M. Powell, and T. Buonassisi, Phys. Status Solidi RRL **7**, 1041 (2013).
[18]Y. M. Yang, A. Yu, B. Hsu, W. C. Hsu, A. Yang, and C. W. Lan, Prog. Photovoltaics **23**, 340 (2015).
[19]C. Donolato, J. Appl. Phys. **84**, 2656 (1998); M. Rinio, A. Yodyungyong, S. Keipert-Colberg, D. Borchert, and A. Montesdeoca-Santana, Phys. Status Solidi A **208**, 760 (2011).
[20]S. Castellanos, M. Kivambe, J. Hofstetter, M. Rinio, B. Lai, and T. Buonassisi, J. Appl. Phys. **115**, 183511 (2014).
[21]D. Macdonald, J. Tan, and T. Trupke, J. Appl. Phys. **103**, 073710 (2008).
[22]D. Macdonald, T. Roth, P. N. K. Deenapanray, T. Trupke, and R. A. Bardos, Appl. Phys. Lett. **89**, 142107 (2006).
[23]D. Macdonald provided calculation spreadsheet.
[24]A. Richter, M. Hermle, and S. W. Glunz, IEEE J. Photovoltaics **3**, 1184 (2013).
[25]A. Cuevas, *QSS-Model v5.2*, 2012.
[26]E. Kobayashi, N. Kusunoki, Y. Watabe, R. Hao, and T. S. Ravi, in *Proceedings of the 6th World Conference on Photovoltaic Energy Conversion*, Kyoto, Japan (2014); E. Kobayashi, Y. Watabe, R. Hao, and T. S. Ravi, Appl. Phys. Lett. **106**, 223504 (2015).
[27]B. A. Komarov, F. P. Korshunov, and L. I. Murin, Fizika i Tekhnika Poluprovodnikov **28**, 499 (English translation: Soviet Physics—Semiconductors **28**, 305–309, 1994); V. P. Markevich, A. R. Peaker, B. Hamilton, S. B. Lastovskii, and L. I. Murin, J. Appl. Phys. **115**, 012004 (2014).
[28]W. Schröter and M. Seibt, in *Properties of Crystalline Silicon*, edited by R. Hull (INSPEC, Short Run Press, Exeter, 1999), p. 561.
[29]M. Pugnet, J. Barbolla, J. C. Brabant, F. Saint-Yves, and M. Brousseau, Phys. Status Solidi A **35**, 533 (1976).
[30]S. D. Brotherton, P. Bradley, and J. Bicknell, J. Appl. Phys. **50**, 3396 (1979).
[31]H. Lemke, Phys. Status Solidi A **101**, 193 (1987).
[32]J. U. Sachse, E. Ö. Sveinbjörnsson, W. Jost, J. Weber, and H. Lemke, Phys. Rev. B **55**, 16176 (1997); J. U. Sachse, J. Weber, and E. Ö. Sveinbjörnsson, *ibid.* **60**, 1474 (1999).
[33]J. Lindroos, D. P. Fenning, D. J. Backlund, E. Verlage, A. Gorgulla, S. K. Estreicher, H. Savin, and T. Buonassisi, J. Appl. Phys. **113**, 204906 (2013).
[34]D. P. Fenning, Ph.D. thesis, Massachusetts Institute of Technology, 2013.
[35]T. Buonassisi, A. A. Istratov, M. Heuer, M. A. Marcus, R. Jonczyk, J. Isenberg, B. Lai, Z. Cai, S. Heald, W. Warta, R. Schindler, G. Willeke, and E. R. Weber, J. Appl. Phys. **97**, 074901 (2005).
[36]J. Hofstetter, Ph.D. thesis, Universidad Politécnica de Madrid, 2011.
[37]O. Tobail, M. Reuter, and J. H. Werner, in *Proceedings of the 24th European Photovoltaic Solar Energy Conference*, Hamburg, Germany (2009), p. 2593.
[38]K. Graff, *Metal Impurities in Silicon-Device Fabrication* (Springer, Berlin, 1999).
[39]A. R. Peaker, V. P. Markevich, B. Hamilton, G. Parada, A. Dudas, A. Pap, E. Don, B. Lim, J. Schmidt, L. Yu, Y. Yoon, and G. Rozgonyi, Phys. Status Solidi A **209**, 1884 (2012).
[40]J. Hofstetter, J.-F. Lelièvre, C. del Cañizo, and A. Luque, Mater. Sci. Eng., B **159–160**, 299 (2009).
[41]T. U. Nærland, L. Arnberg, and A. Holt, Prog. Photovoltaics **17**, 289 (2009).
[42]A. Haarahiltunen, H. Väinölä, M. Yli-Koski, J. Sinkkonen, and O. Anttila, ECS Trans. **3**, 273 (2006).
[43]J. Hofstetter, D. P. Fenning, J.-F. Lelièvre, C. del Cañizo, and T. Buonassisi, Phys. Status Solidi A **209**, 1861 (2012).
[44]A. Bentzen, A. Holt, R. Kopecek, G. Stokkan, J. S. Christensen, and B. G. Svensson, J. Appl. Phys. **99**, 093509 (2006).
[45]T. S. Ravi, "Technology development for high-efficiency solar cells and modules using thin (<80 μm) single-crystal silicon wafers produced by epitaxy," NREL Subcontract Report No. NREL/SR-5200-58593, 2013.
[46]D. M. Powell, Ph.D. thesis, Massachusetts Institute of Technology, 2014.

[47]M. M'Hamdi, E. A. Meese, H. Laux, and E. J. Øvrelid, Mater. Sci. Forum **508**, 597 (2006).
[48]F. S. Ham, J. Phys. Chem. Solids **6**, 335 (1958).
[49]H. Hieslmair, A. A. Istratov, T. Heiser, and E. R. Weber, J. Appl. Phys. **84**, 713 (1998).
[50]D. Macdonald, A. Cuevas, A. Kinomura, Y. Nakano, and L. J. Geerligs, J. Appl. Phys. **97**, 033523 (2005).
[51]H. Hieslmair, A. A. Istratov, S. A. McHugo, C. Flink, T. Heiser, and E. R. Weber, Appl. Phys. Lett. **72**, 1460 (1998).
[52]S. A. McHugo, H. Hieslmair, and E. R. Weber, Appl. Phys. A **64**, 127–137 (1997).
[53]J. Hofstetter, C. del Cañizo, H. Wagner, S. Castellanos, and T. Buonassisi, Prog. Photovoltaics **24**, 122 (2016).
[54]M. A. Jensen, J. Hofstetter, A. E. Morishige, G. Coletti, B. Lai, D. P. Fenning, and T. Buonassisi, Appl. Phys. Lett. **106**, 202104 (2015).
[55]A. E. Morishige, D. P. Fenning, J. Hofstetter, M. A. Jensen, S. Ramanathan, C. Wang, B. Lai, and T. Buonassisi, in *Proceedings of the 40th Photovoltaic Specialist Conference (PVSC)*, Denver, CO, USA (2014), pp. 3004–3007.
[56]J. Schön, A. Haarahiltunen, H. Savin, D. P. Fenning, T. Buonassisi, W. Warta, and M. C. Schubert, IEEE J. Photovoltaics **3**, 131–137 (2013).
[57]A. Haarahiltunen, H. Savin, M. Yli-Koski, H. Talvitie, M. I. Asghar, and J. Sinkkonen, Mater. Sci. Eng., B **159–160**, 248–252 (2009).
[58]A. E. Morishige, H. S. Laine, J. Schön, A. Haarahiltunen, J. Hofstetter, C. del Cañizo, M. C. Schubert, H. Savin, and T. Buonassisi, Appl. Phys. A **120**, 1357–1373 (2015).